

Unsupervised Topological Phase Discovery in Periodically Driven Systems via Floquet-Bloch State

Chen-Yang Wang, Jing-Ping Xu, Ce Wang,* and Ya-Ping Yang

School of Physics Science and Engineering, Tongji University, Shanghai 200092, China

Floquet engineering offers an unparalleled platform for realizing novel non-equilibrium topological phases. However, the unique structure of Floquet systems, which includes multiple quasienergy gaps, poses a significant challenge to classification using conventional analytical methods. We propose a novel unsupervised machine learning framework that employs a kernel defined in momentum-time (\mathbf{k}, t) space, constructed directly from Floquet-Bloch eigenstates. This approach is intrinsically data-driven and requires no prior knowledge of the underlying topological invariants, providing a fundamental advantage over prior methods that rely on abstract concepts like the micromotion operator or homotopic transformations. Crucially, this work successfully reveals the intrinsic topological characteristics encoded within the Floquet eigenstates themselves. We demonstrate that our method robustly and simultaneously identifies the topological invariants associated with both the 0-gap and the π -gap across various symmetry classes (1D AIII, 1D D, and 2D A), establishing a robust methodology for the systematic classification and discovery of complex non-equilibrium topological matter.

Introduction-Topological condensed matter physics has achieved landmark progress in recent decades, with its core lying in the robust edge states protected by topological invariants and bulk energy gaps [1–12]. While traditional classification schemes primarily focused on equilibrium systems described by static (time-independent) Hamiltonians, the rapid development of experimental techniques has spurred interest in extending topological concepts to non-equilibrium states. This is particularly exemplified by time-periodically driven systems, known as Floquet systems [13–28].

Floquet engineering provides a powerful paradigm for the active manipulation and design of quantum matter. By applying periodic external driving, the system's dynamics can be described by a time-independent effective Hamiltonian. The spectrum of this Hamiltonian is composed of quasi-energies, the inherent periodicity of which brings a rich topological structure far beyond that of static Hamiltonians. A notable feature is the emergence of non-trivial topological edge states even when the effective (time-averaged) Hamiltonian is trivial [20].

The unparalleled designability of Floquet systems, achieved by tuning periodic driving parameters, offers unprecedented possibilities for realizing novel non-equilibrium topological phases. However, this richness brings classification challenges that exceed those of static systems. Specifically, the quasi-energy spectrum's periodicity introduces multiple independent and interrelated topological gaps, and the highly nonlinear dependence of the phase diagram on driving parameters makes systematic exploration using traditional analytical or numerical methods inherently difficult [22, 27].

This is where unsupervised learning provides a crucial advantage. The task of identifying phase transitions and classifying phases of matter using unsupervised methods has become a rapidly developing and vital area of research [29–47]. Early efforts in this field used tech-

niques like Principal Component Analysis (PCA) to successfully identify phase transitions in classical statistical models [36–38]. Subsequently, advanced manifold learning methods, such as diffusion maps, demonstrated success in clustering topological phases based on state information [39–47]. A major, more recent advancement involves using kernel methods based on projection operators for the non-iterative clustering of gapped quantum systems [46].

Inspired by these powerful, emerging approaches, we extend the efficient kernel-based unsupervised learning framework to address the complexities of Floquet topological systems. We introduce a novel kernel defined directly in the momentum-time (\mathbf{k}, t) space. This kernel is designed to effectively quantify the topological similarity between Floquet Hamiltonians by evaluating the geometric structure of their eigenstates. A prior unsupervised approach for Floquet topological insulators relied on the abstract and computationally involved micromotion operator and specific homotopic transformations, often demanding prior knowledge of the system [47]. **In sharp contrast**, our \mathbf{k}, t -space kernel utilizes information directly from the Floquet eigenstates, offering a computationally efficient and fundamental data-driven methodology that requires no reliance on the micromotion operator, homotopic transformations, or any prior topological invariant knowledge.

We demonstrate that our kernel enables the robust, simultaneous identification of the topological invariants of the phases associated with both the 0-gap and the π -gap across different symmetry classes (AIII, D, and A). Our results establish a clear data-driven approach for identifying Floquet phases. We further show that the Floquet eigenstates in \mathbf{k}, t -space inherently encode the topological information for both gaps simultaneously. This framework can be readily extended to classify other complex Floquet topological systems.

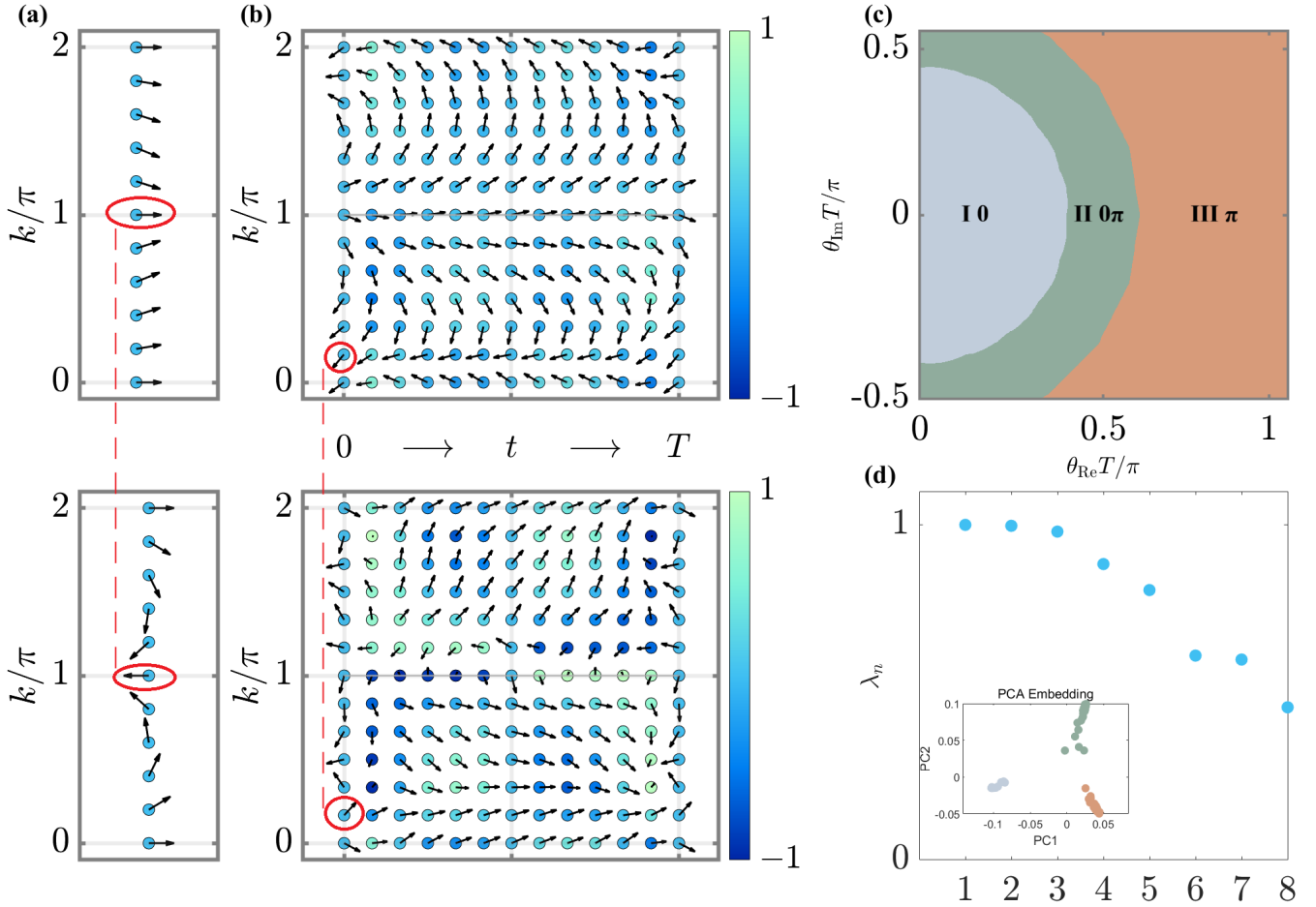


FIG. 1. (a) Two static topological systems possessing distinct topological numbers must necessarily exhibit band inversion points. The top and bottom figures illustrate the Bloch vector representations for the topologically trivial and non-trivial phases, respectively, in the SSH model. (b) The Bloch vector representations for the *flattened Floquet operator* for the modulated Floquet SSH model. The top configuration is sampled from the 0-phase ($\theta_{\text{Re}} = 0.2\pi/T, \theta_{\text{Im}} = 0.2\pi/T$) and the bottom configuration is sampled from the π -phase ($\theta_{\text{Re}} = 0.6\pi/T, \theta_{\text{Im}} = 0.2\pi/T$). The colorbar describes the z -component of the Bloch vector. (c) The phase diagram is derived using the unsupervised clustering algorithm. Comparing the result with the theoretical topological numbers, we observe that Phase I has $W_0 = 1, W_\pi = 0$, Phase II has $W_0 = 1, W_\pi = 1$ and Phase III has $W_0 = 0, W_\pi = 1$. (d) The eigenvalues output by the diffusion map algorithm, where three eigenvalues close to 1 indicate that the data has been partitioned into three clusters. The inset shows the two-dimensional projection of the dataset in the principal component space after sufficient diffusion.

Method - First, we review the core concept of unsupervised topological classification for static bands: For any two topologically distinct bands, there exists a momentum \mathbf{k} where the sum of their corresponding *flattened Hamiltonians* yields at least one zero eigenvalue [46]. This is schematically illustrated for the static Su–Schrieffer–Heeger (SSH) model [10–12] in Fig. 1(a), where the flatten Hamiltonian corresponds to the Bloch vector. Crucially, configurations with distinct winding numbers exhibit antiparallel Bloch vectors at certain momentum points. Building on this observation, one can design a kernel function that assigns larger values when the determinant of the summation vanishes at a given \mathbf{k} -point, and smaller values otherwise. The topological

classification of data sets is subsequently achieved by integrating this kernel with an appropriate unsupervised clustering algorithm [46].

We now extend this idea to Floquet systems. The eigenmode of a periodically driven lattice can be represented by the **Floquet-Bloch state** [18, 26] $|\phi_n(\mathbf{k}, t)\rangle$ with

$$\left(H(\mathbf{k}, t) - i \frac{\partial}{\partial t} \right) |\phi_n(\mathbf{k}, t)\rangle = \epsilon_n(\mathbf{k}) |\phi_n(\mathbf{k}, t)\rangle, \quad (1)$$

where $H(\mathbf{k}, t) = H(\mathbf{k}, t+T)$ is the Hamiltonian, n is the band index and $\epsilon_n(\mathbf{k}) \in [-\pi/T, \pi/T]$ is the quasi-energy of n -th band (out of a total of N_b bands). We define the

flattened Floquet operator (FFO) as

$$Q(\mathbf{k}, t) = 1 - 2 \sum_{n \in occ} |\phi_n(\mathbf{k}, t)\rangle \langle \phi_n(\mathbf{k}, t)|, \quad (2)$$

where occ means the occupied Floquet bands. Crucially, we demonstrate through various examples that the topology of Floquet-Bloch states is profoundly linked to specific-gap Floquet topological invariants. Consequently, the FFO plays an analogous role to the flattened Hamiltonian in static systems: For any two topologically distinct Floquet bands, there exists a spacetime point (\mathbf{k}, t) where the sum of their corresponding FFOs yields at least one zero eigenvalue. As shown in Fig. 1(a,b), we have encircled the spin-flip points in red. At these spin-flip points, one eigenvalue of FFO becomes zero.

To achieve unsupervised classification of Floquet Hamiltonians randomly sampled in the parameter space, we define the kernel matrix:

$$K_{ij} = \prod_{\substack{\mathbf{k} \in \text{BZ} \\ t \in [0, T]}} \left(1 - \exp \left[- \left| \frac{\det(Q^{(i)}(\mathbf{k}, t) + Q^{(j)}(\mathbf{k}, t))}{\epsilon} \right|^2 \right] \right), \quad (3)$$

where superscripts i, j index distinct parameter configurations and $\epsilon \rightarrow 0^+$ is a sufficiently small positive constant that ensures K_{ij} can be approximately treated as a binary step function. This matrix quantifies pairwise topological similarities among N sampled Hamiltonians, satisfying $K_{ij} \rightarrow 0$ for topologically inequivalent pairs.

To classify the dataset into topologically distinct clusters, we implement the *diffusion map* algorithm by constructing the probability transition matrix $P_{ij} = K_{ij} / \sum_{j'} K_{ij'}$. The diffusion distance [39–47] between samples i and j after ℓ steps is given by:

$$d_{ij}^{(\ell)} = \sqrt{\sum_{n=0}^{N-1} \lambda_n^{2\ell} [(v_n)_i - (v_n)_j]^2} \quad (4)$$

where v_n is the n th right eigenvector of the normalized transition matrix \hat{P} with corresponding eigenvalue λ_n ($n = 0, 1, \dots, N-1$), ordered such that $1 = \lambda_0 \geq \lambda_1 \geq \dots \geq \lambda_{N-1} \geq 0$. Under prolonged diffusion ($\ell \gg 1$), the dominant contributions arise from the eigenvectors v_n with $\lambda_n \approx 1$. These components encode the essential topological features of the diffusion manifold, forming a low-dimensional representation of the original FFO data. Topological classification is then derived by clustering this reduced representation.

Next, we apply this framework to Floquet systems across different symmetry classes.

AIII class in one-dimension - As a concrete example, we consider the modulated Floquet SSH model in symmetry class AIII, described by the Hamiltonian [21, 22, 28]:

$$H(k, t) = \theta_{\text{Re}} \sigma_x + \theta_{\text{Im}} \sigma_y + \gamma(t) [\cos(k) \sigma_x + \sin(k) \sigma_y], \quad (5)$$

where θ_{Re} and θ_{Im} represent the real and imaginary parts of the intracell coupling, $\gamma(t) = 0.6\pi/T + 2g \cos(\omega t)$ is a periodically oscillating even function that models the intercell coupling, and $\sigma_x, \sigma_y, \sigma_z$ are the Pauli matrices. A key aspect of this model is the inclusion of an imaginary intercell coupling, which explicitly breaks time-reversal and particle-hole symmetries. This symmetry breaking removes high-symmetry points along the momentum direction, thereby substantially enriching the diversity and generality of the dataset. The system retains chiral symmetry [26], defined by $\mathcal{S}^{-1}H(k, t)\mathcal{S} = -H(k, -t)$ with $\mathcal{S} = \sigma_z$.

The topological properties of the two-band Floquet model are characterized by two topological invariants, W_0 and W_π , which describe the topology associated with the 0-gap and π -gap, respectively. These are related to the winding numbers ν_0 and $\nu_{T/2}$ of the Floquet-Bloch state $|\phi_-(k, 0)\rangle$ and $|\phi_-(k, T/2)\rangle$ along the k -axis via (the quasi-energy of occupied bands satisfies $-\pi/T < \epsilon_-(k) < 0$):

$$W_0 = \frac{1}{2}(\nu_0 + \nu_{T/2}), \quad W_\pi = \frac{1}{2}(\nu_{T/2} - \nu_0). \quad (6)$$

Thus, any two configurations with distinct values of W_0 or W_π must also differ in ν_0 or $\nu_{T/2}$. A detailed proof is provided in the appendix [48]. This guarantees the existence of at least one spacetime point (k, t) where the sum of the corresponding FFOs yields exactly one zero eigenvalue. As illustrated in Fig. 1(b), the FFO configuration (top) where $W_0 = 1$ and $W_\pi = 0$ corresponds to $\nu_0 = \nu_{T/2} = 1$, while the configuration (bottom) where $W_0 = 0$ and $W_\pi = 1$ corresponds to $\nu_0 = -1$ and $\nu_{T/2} = 1$. Therefore, their FFOs should exhibit different winding numbers along the k direction in $Q(k, 0)$, which will consequently lead to the appearance of opposite Bloch vectors.

We then constructed the dataset by sweeping the real and imaginary components of θ and analyzed it using our clustering algorithm. The spectral analysis of the diffusion map kernel, presented in Fig. 1(d), reveals three dominant eigenvalues near unity, signifying the data is partitioned into three distinct clusters. Theoretical verification confirmed that these clusters map precisely to unique topological invariants, thereby demonstrating the algorithm's accuracy in identifying the topological phase diagram for this parameter region [Fig. 1(c)].

A class in two-dimension - To highlight the generalization capability of our approach, we examine the two-dimensional A-class [20, 25, 26]. Specifically, we focus on

the following famous Floquet Bloch Hamiltonian:

$$H(\mathbf{k}, t) = \begin{cases} J\sigma_x + \delta\sigma_z, & 0 \leq t < \frac{T}{5} \\ J(e^{i(k_x - k_y)}\sigma^+ + \text{H.c.}) + \delta\sigma_z, & \frac{T}{5} \leq t < \frac{2T}{5} \\ J(e^{i(2k_x)}\sigma^+ + \text{H.c.}) + \delta\sigma_z, & \frac{2T}{5} \leq t < \frac{3T}{5} \\ J(e^{i(k_x + k_y)}\sigma^+ + \text{H.c.}) + \delta\sigma_z, & \frac{3T}{5} \leq t < \frac{4T}{5} \\ \delta\sigma_z, & \frac{4T}{5} \leq t \leq T \end{cases} \quad (7)$$

In real space, the Hamiltonian describes a periodically driven process on a square lattice as shown in Fig. 3(a). The hopping with strength J , is sequentially activated along each bond. This occurs in a clockwise sequence, with each activation lasting $T/5$. For the final $T/5$ of the period, all coupling is switched off. Additionally, a

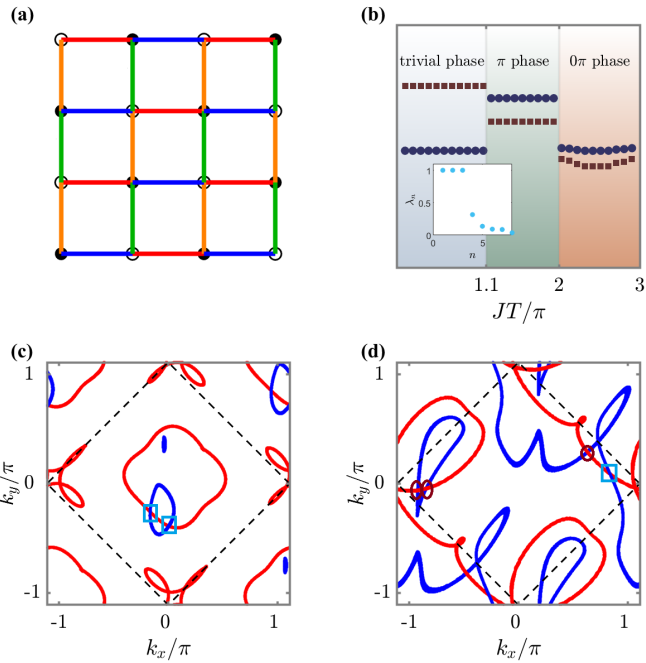


FIG. 2. (a) Schematic illustration of the 2D modulated Floquet model, where different colors indicate the coupling between lattice sites in different time segments. The interatomic couplings evolve in a clockwise sequence following the order red, green, blue, and orange. (b) Phase diagram obtained using an unsupervised clustering algorithm. By comparing the clustering results with the theoretical topological invariants, three distinct phases are identified: the trivial phase with $W_0 = 0$, $W_\pi = 0$; the π phase with $W_0 = 0$, $W_\pi = 1$; and the 0π phase with $W_0 = 1$, $W_\pi = 1$. (c,d) Inverse images of two Bloch vectors \mathbf{n} and $-\mathbf{n}$ of the Floquet–Bloch states. The first Brillouin zone is indicated by the dashed lines; the linking number is 0 in (c) and 1 in (d). (orientation of the Bloch vector $x = \cos(\theta)\sin(\phi)$, $y = \sin(\theta)\sin(\phi)$, $z = \cos(\phi)$, the red line: $\phi = \pi$, the blue line: $\theta = \pi$, $\phi = 0.75\pi$.) (c) corresponds to the case with $J = 0.4\pi/T$, $W_0 = 0$, $W_\pi = 0$, where the linking number of the preimages is 0; (d) corresponds to $J = 2.7\pi/T$, $W_0 = 1$, $W_\pi = 1$, where the linking number of the preimages is 1.

staggered on-site potential, with strength 2δ , is continuously applied to the A and B sublattices. This model belongs to the two-dimensional A-class, since it lacks time-reversal (\mathcal{T}), particle-hole (\mathcal{P}), and chiral (\mathcal{S}) symmetries [26]. Its topological properties are characterized by two independent topological invariants, W_0 and W_π , corresponding to the quasienergy gaps at 0 and π/T , respectively.

To explore different topological phases of this model, we fix $\delta = 0.5\pi/T$ and generate the FFO data for the occupied band ($-\pi/T < \epsilon(\mathbf{k}) < 0$) with different J which is uniformly sampled from 0 to $3\pi/T$. The output of the diffusion map algorithm is presented in Fig. 3(b). The presence of three dominant eigenvalues near unity signifies that the dataset is partitioned into three distinct clusters. Crucially, the clustering results exhibit excellent agreement with the three phases defined by W_0 and W_π : the trivial phase ($W_0 = 0, W_\pi = 0$), the π -phase ($W_0 = 0, W_\pi = 1$) and the 0π -phase ($W_0 = 1, W_\pi = 1$).

We then investigate how the Floquet–Bloch states encode the distinct topological phases. Similar to the case studied previously, there should exist two topological invariants of $|\phi_-(\mathbf{k}, t)\rangle$ that form a bijection with W_0, W_π .

The first invariant is the Chern number C of $|\phi_-(\mathbf{k}, t)\rangle$ in the (k_x, k_y) plane at fix t , which is given by the following relation [20, 25, 26]:

$$C = W_0 - W_\pi. \quad (8)$$

Thus, the FFO corresponding to the π -phase data possesses a non-trivial Chern number, $C = -1$, for all (k_x, k_y) planes. Conversely, the FFO for the trivial or 0π -phase data yields $C = 0$. Consequently, the π -phase FFO data can be distinguished from the other ones.

The second invariant is the Pontryagin's ν invariant. When $C = 0$, ν reduces to the Hopf invariant [49, 50]. The Hopf invariant is geometrically defined as the linking number of the trajectories formed by the pre-images of two fixed Bloch vectors in the three-dimensional (k_x, k_y, t) parameter space. As shown in Fig. 3(c,d), we calculate the linking number by counting the number of times the red and blue trajectories cross each other, within the first Brillouin zone marked by the dashed lines, the red circle indicates that the red trajectory is above, and the blue box indicates that the blue trajectory is above. For trivial phase, two trajectories do not link with each other, while in 0π -phase the linking number is 1. The difference in the Hopf invariant explains how the algorithm distinguishes trivial phase from 0π -phase. We find that for general case, the Pontryagin's invariant [51, 52] is given by [48]:

$$\nu = W_\pi \bmod 2(W_\pi - W_0). \quad (9)$$

It is worth noting that this relation provides an elegant method to calculate the Pontryagin's invariant for quantum quench problems with topological non-trivial

initial states, which becomes complicated by the gauge dependence of the Chern-Simons integral. The detail of Pontryagin's is provided in the appendix [48].

D class in one-dimension - The third model we study belongs to symmetry class D and is described by the Hamiltonian [27]:

$$H(k, t) = \begin{cases} -J_1[\sin(k)\sigma_x - \cos(k)\sigma_y] + g\sin(k)\sigma_z, & t \leq \frac{T}{2} \\ J_2\sigma_y + g\sin(k)\sigma_z, & \frac{T}{2} < t \leq T \end{cases} \quad (10)$$

where J_1 and J_2 represent the strengths of nearest spin interactions. The parameter g breaks both chiral and time-reversal symmetries. The system retains particle-hole symmetry [26, 27], defined by $\mathcal{C}^{-1}H(k, t)\mathcal{C} = -H^*(-k, t)$ with $\mathcal{C} = I$.

In contrast to the \mathbb{Z} -type invariants of the previous models, the one-dimensional D Class system is characterized by a \mathbb{Z}_2 invariant, indicating two states for each quasienergy gap: trivial ($V_{0/\pi} = +1$) or nontrivial ($V_{0/\pi} = -1$). In static 1D D Class systems, the topo-

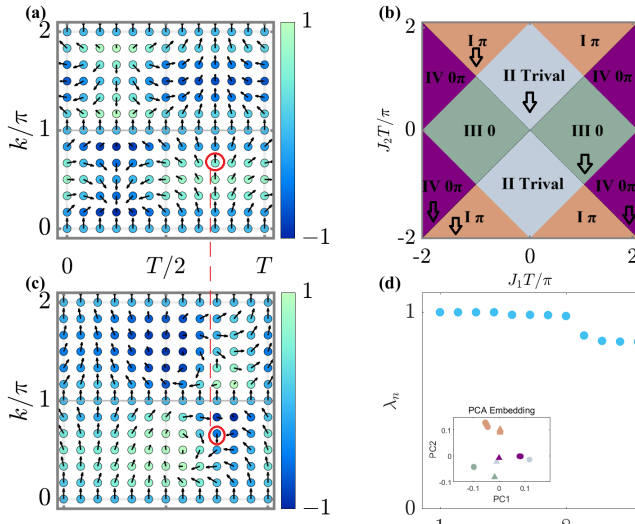


FIG. 3. (a) (c) The Bloch vector representations for the FFO for the modulated Floquet D model. The configuration in (a) is sampled from the Trivial-phase ($J_1 = 0, J_2 = -\pi/T$) and the configuration in (c) is sampled from the 0π -phase ($J_1 = 1.5\pi/T, J_2 = \pi/T$). The colorbar describes the z -component of the Bloch vector. The red circles mark the flipping points identified by the FFO. (b) displays the phase diagram of the model, where the downward arrows indicate phases in which the Bloch vector at the high-symmetry point $k = 0$ points along the negative y direction. (d) The eigenvalues output by the diffusion map algorithm, where eight eigenvalues close to 1 indicate that the data has been partitioned into eight clusters. The inset shows the two-dimensional projection of the dataset in the principal component space after sufficient diffusion. In the inset the triangles mark the phases in which the Bloch vector at the high-symmetry point $k = 0$ points along the negative y direction.

logical invariant is determined solely by the orientations of the Bloch vectors at the high-symmetry points $k = 0$ and $k = \pi$. For this Floquet system, we find the relation between the topology of Floquet-Bloch state and $V_{0/\pi}$ is given by [48]

$$V_0V_\pi = 2|\langle\phi_-(\pi, t)|\phi_-(0, t)\rangle|^2 - 1, V_\pi = (-1)^{C_h}, \quad (11)$$

where $C_h = \frac{1}{\pi} \int_0^T dt \int_0^\pi dk \text{Im} \langle \partial_t \phi_-(k, t) | \partial_k \phi_-(k, t) \rangle$ [53]. This implies that the orientations of the Bloch vectors at the high-symmetry lines $k = 0$ and $k = \pi$ only determine the product V_0V_π , whereas the parity of C_h dictates the triviality or nontriviality of V_π . C_h has been discussed in D-class adiabatic pumps [54]. As shown in Fig. 3(a,c), the FFO reliably distinguishes the trivial phase and the 0π phase via the distinct C_h values, even when their high-symmetry point orientations are identical.

We consider a dataset uniformly sampled from the parameter region $J_1T/\pi \in [-2, 2]$, $J_2T/\pi \in [-2, 2]$ and $g = 0.5\pi/T$. Our algorithm ultimately classifies the data into eight distinct groups, as indicated by the eight nearly unitary eigenvalues shown in Fig. 3(d). These eight clusters correspond to the four theoretical phases shown in Fig. 3(b). The splitting of a single topological phase into two distinct subclasses occurs because the algorithm identifies different high-symmetry point orientations at $k = 0$ and $k = \pi$ as separate groups, even when they map to the same (V_0, V_π) invariant pair. Such additional sub-classifications are often unavoidable in automated symmetry-protected clustering, similar phenomenon has been observed in Ref. [46].

Conclusions and Discussion— In summary, we have proposed an unsupervised approach for classifying Floquet topological phases based on FFO. By validating the method in three representative models—the one-dimensional AIII class, the one-dimensional D class, and the two-dimensional A class—we demonstrate its universality. This method allows us to study the topological classification of Floquet systems without requiring any prior knowledge of topological invariants, and they further reveal essential differences between Floquet topological phases and their static counterparts.

We also identify a correlation between the topological properties of Floquet-Bloch states and those of the quasienergy gaps. Moreover, the relation between the topological invariants of Floquet-Bloch states and gap topological invariants deserves further investigation. For instance, in the two-dimensional A class, distinct gap topological invariants may arise even when the Floquet-Bloch states share the same topological phase [48]. Similarly, in the one-dimensional D class, while the parity of the half-Brillouin-zone Chern number determines V_π , it remains unknown whether two configurations with the same parity of C_h are homotopically connected. This raises the broader question of whether the topological properties of Floquet gaps necessarily coincide with those of the corresponding Floquet-Bloch states.

Acknowledgments—This work is supported by the National Natural Science Foundation of China(NSFC) under Grant Nos.12204352(CW) and the National Natural Science Foundation of China (Grants No. 12174288 and No.12274326) and the National Key R & D Program of China(Grant No. 2021YFA1400602).

* cewang@tongji.edu.cn

- [1] X.-L. Qi and S.-C. Zhang, Topological insulators and superconductors, *Rev. Mod. Phys.* **83**, 1057 (2011).
- [2] Y. Liu, Y. Xu, S.-C. Zhang, and W. Duan, Model for topological phononics and phonon diode, *Phys. Rev. B* **96**, 064106 (2017).
- [3] J. Lu, C. Qiu, L. Ye, X. Fan, M. Ke, F. Zhang, and Z. Liu, Observation of topological valley transport of sound in sonic crystals, *Nat. Phys.* **13**, 369 (2017).
- [4] L. Lu, J. D. Joannopoulos, and M. Soljačić, Topological photonics, *Nat. Photonics* **8**, 248 (2014).
- [5] J. Deng, H. Dong, C. Zhang, Y. Wu, J. Yuan, X. Zhu, F. Jin, H. Li, Z. Wang, H. Cai, C. Song, H. Wang, J. Q. You, and D.-W. Wang, Observing the quantum topology of light, *Science* **378**, 966 (2022).
- [6] T. Ozawa, H. M. Price, A. Amo, N. Goldman, M. Hafezi, L. Lu, M. C. Rechtsman, D. Schuster, J. Simon, O. Zilberman, and I. Carusotto, Topological photonics, *Rev. Mod. Phys.* **91**, 015006 (2019).
- [7] C. L. Kane and E. J. Mele, Quantum spin hall effect in graphene, *Phys. Rev. Lett.* **95**, 226801 (2005).
- [8] B. A. Bernevig, T. L. Hughes, and S.-C. Zhang, Quantum spin hall effect and topological phase transition in hgte quantum wells, *Science* **314**, 1757 (2006).
- [9] F. D. M. Haldane, Model for a quantum hall effect without landau levels: Condensed-matter realization of the “parity anomaly”, *Phys. Rev. Lett.* **61**, 2015 (1988).
- [10] C. Poli, M. Bellec, U. Kuhl, F. Mortessagne, and H. Schomerus, Selective enhancement of topologically induced interface states in a dielectric resonator chain, *Nat. Commun.* **6**, 6710 (2014).
- [11] W. P. Su, J. R. Schrieffer, and A. J. Heeger, Solitons in polyacetylene, *Phys. Rev. Lett.* **42**, 1698 (1979).
- [12] L. Li, Z. Xu, and S. Chen, Topological phases of generalized su-schrieffer-heeger models, *Phys. Rev. B* **89**, 085111 (2014).
- [13] R. Roy and F. Harper, Periodic table for floquet topological insulators, *Phys. Rev. B* **96**, 155118 (2017).
- [14] T. Kitagawa, E. Berg, M. Rudner, and E. Demler, Topological characterization of periodically driven quantum systems, *Phys. Rev. B* **82**, 235114 (2010).
- [15] A. Gómez-León and G. Platero, Floquet-bloch theory and topology in periodically driven lattices, *Phys. Rev. Lett.* **110**, 200403 (2013).
- [16] N. H. Lindner, G. Refael, and V. Galitski, Floquet topological insulator in semiconductor quantum wells, *Nature Physics* **7**, 490–495 (2011).
- [17] N. Lambert, C. Emery, and T. Brandes, Entanglement and the phase transition in single-mode superradiance, *Phys. Rev. Lett.* **92**, 073602 (2004).
- [18] M. S. Rudner and N. H. Lindner, Band structure engineering and non-equilibrium dynamics in floquet topological insulators, *Nat. Rev. Phys.* **2**, 229 (2020).
- [19] M. Z. Hasan and C. L. Kane, Colloquium: Topological insulators, *Rev. Mod. Phys.* **82**, 3045 (2010).
- [20] M. S. Rudner, N. H. Lindner, E. Berg, and M. Levin, Anomalous edge states and the bulk-edge correspondence for periodically driven two-dimensional systems, *Phys. Rev. X* **3**, 031005 (2013).
- [21] Q. Cheng, Y. Pan, H. Wang, C. Zhang, D. Yu, A. Gover, H. Zhang, T. Li, L. Zhou, and S. Zhu, Observation of anomalous π modes in photonic floquet engineering, *Phys. Rev. Lett.* **122**, 173901 (2019).
- [22] V. Dal Lago, M. Atala, and L. E. F. Foa Torres, Floquet topological transitions in a driven one-dimensional topological insulator, *Phys. Rev. A* **92**, 023624 (2015).
- [23] L. Jiang, T. Kitagawa, J. Alicea, A. R. Akhmerov, D. Pekker, G. Refael, J. I. Cirac, E. Demler, M. D. Lukin, and P. Zoller, Majorana fermions in equilibrium and in driven cold-atom quantum wires, *Phys. Rev. Lett.* **106**, 220402 (2011).
- [24] G. B. Mbeng, A. Russomanno, and G. E. Santoro, The quantum Ising chain for beginners, *SciPost Phys. Lect. Notes* , 82 (2024).
- [25] F. Nathan and M. S. Rudner, Topological singularities and the general classification of floquet–bloch systems, *New Journal of Physics* **17**, 125014 (2015).
- [26] S. Yao, Z. Yan, and Z. Wang, Topological invariants of floquet systems: General formulation, special properties, and floquet topological defects, *Phys. Rev. B* **96**, 195303 (2017).
- [27] P. Xu and T.-S. Deng, Boundary discrete time crystals induced by topological superconductors in solvable spin chains, *Phys. Rev. B* **107**, 104301 (2023).
- [28] M. Ghuneim and R. W. Bomantara, Anomalous topological edge modes in a periodically driven trimer lattice, *Phys. Rev. B* **111**, 195424 (2025).
- [29] A. Decelle, B. Seoane, and L. Rosset, Unsupervised hierarchical clustering using the learning dynamics of restricted boltzmann machines, *Phys. Rev. E* **108**, 014110 (2023).
- [30] S. J. Wetzel, Unsupervised learning of phase transitions: From principal component analysis to variational autoencoders, *Phys. Rev. E* **96**, 022140 (2017).
- [31] V. Mikuni and F. Canelli, Unsupervised clustering for collider physics, *Phys. Rev. D* **103**, 092007 (2021).
- [32] X. Xu, Q. Wei, H. Li, Y. Wang, Y. Chen, and Y. Jiang, Recognition of polymer configurations by unsupervised learning, *Phys. Rev. E* **99**, 043307 (2019).
- [33] D. S. Berman, Y.-H. He, and E. Hirst, Machine learning calabi-yau hypersurfaces, *Phys. Rev. D* **105**, 066002 (2022).
- [34] D. George, H. Shen, and E. A. Huerta, Classification and unsupervised clustering of ligo data with deep transfer learning, *Phys. Rev. D* **97**, 101501 (2018).
- [35] A. Jaiswal, T. Egami, and Y. Zhang, Atomic-scale dynamics of a model glass-forming metallic liquid: Dynamical crossover, dynamical decoupling, and dynamical clustering, *Phys. Rev. B* **91**, 134204 (2015).
- [36] J. Carrasquilla and R. G. Melko, Machine learning phases of matter, *Nat. Phys.* **13**, 431 (2017).
- [37] C. Wang and H. Zhai, Machine learning of frustrated classical spin models (ii): Kernel principal component analysis, *Front. Phys.* **13**, 130507 (2018).
- [38] C. Wang and H. Zhai, Machine learning of frustrated classical spin models. i. principal component analysis, *Phys. Rev. B* **96**, 144432 (2017).

[39] L. Wang, Discovering phase transitions with unsupervised learning, *Phys. Rev. B* **94**, 195105 (2016).

[40] M. S. Scheurer and R.-J. Slager, Unsupervised machine learning and band topology, *Phys. Rev. Lett.* **124**, 226401 (2020).

[41] Y. Long, J. Ren, and H. Chen, Unsupervised manifold clustering of topological phononics, *Phys. Rev. Lett.* **124**, 185501 (2020).

[42] L.-W. Yu and D.-L. Deng, Unsupervised learning of non-hermitian topological phases, *Phys. Rev. Lett.* **126**, 240402 (2021).

[43] A. Lidiak and Z. Gong, Unsupervised machine learning of quantum phase transitions using diffusion maps, *Phys. Rev. Lett.* **125**, 225701 (2020).

[44] J. R. Nieva and M. S. Scheurer, Identifying topological order through unsupervised machine learning, *Nat. Phys.* **15**, 790 (2019).

[45] Y. Long, H. Xue, and B. Zhang, Unsupervised learning of topological non-abelian braiding in non-hermitian bands, *Nat. Mach. Intell.* **6**, 904 (2024).

[46] Y. Long and B. Zhang, Unsupervised data-driven classification of topological gapped systems with symmetries, *Phys. Rev. Lett.* **130**, 036601 (2023).

[47] N. Ma and J. Gong, Unsupervised identification of floquet topological phase boundaries, *Phys. Rev. Res.* **4**, 013234 (2022).

[48] C.-Y. Wang, J.-P. Xu, C. Wang, and Y.-P. Yang, Supplemental Material accompanying: *Unsupervised Topological Phase Discovery in Periodically Driven Systems via Floquet-Bloch State*.

[49] C. Wang, P. Zhang, X. Chen, J. Yu, and H. Zhai, Scheme to measure the topological number of a chern insulator from quench dynamics, *Phys. Rev. Lett.* **118**, 185701 (2017).

[50] H. Hu and E. Zhao, Topological invariants for quantum quench dynamics from unitary evolution, *Phys. Rev. Lett.* **124**, 160402 (2020).

[51] X. Chen, C. Wang, and J. Yu, Linking invariant for the quench dynamics of a two-dimensional two-band chern insulator, *Phys. Rev. A* **101**, 032104 (2020).

[52] R. Kennedy, Topological hopf-chern insulators and the hopf superconductor, *Phys. Rev. B* **94**, 035137 (2016).

[53] C. Yang, L. Li, and S. Chen, Dynamical topological invariant after a quantum quench, *Phys. Rev. B* **97**, 060304 (2018).

[54] J. C. Y. Teo and C. L. Kane, Topological defects and gapless modes in insulators and superconductors, *Phys. Rev. B* **82**, 115120 (2010).